Supporting Information

Single Atomic Fe–N$_4$ Active Sites and Neighboring Graphitic Nitrogen for Efficient and Stable Electrochemical CO$_2$ Reduction

Leta Takele Menisa[a,c,‡], Ping Cheng[b‡], Xueying Qiu[a], Yonglong Zheng[a,d],

Xuewei Huang[a,e], Yan Gao [a*] and Zhiyong Tang [a,*]

[a]*CAS Key Laboratory of Nanosystem and Hierarchical Fabrication, CAS Center for Excellence in Nanoscience, National Center for Nanoscience and Technology, Beijing, 100190, P. R. China.*

[b]*College of Science, University of Shanghai for Science and Technology, Shanghai 200093, China* [d]*School of Materials Science and Engineering, Harbin Institute of Technology, Harbin 150080, China*

[c]*College of Natural and Computational Sciences, Department of Chemistry, Haramaya University, P.O. Box 138, Dire Dawa, Ethiopia*

[d]*Institute of Advanced Synthesis (IAS), and School of Chemistry and Molecular Engineering, Jiangsu National Syner-getic Innovation Centre for Advanced Materials, Nanjing Tech University, 211816, Nanjing, China.*

[e]*Green Catalysis Center, and College of Chemistry, Zhengzhou University, Zhengzhou, Henan 450001, P. R. China*

1. Experimental Section

Chemicals: Carbon black BP2000 was purchased from Asian-Pacific Specialty Chemicals Kuala Lumpur, Potassium chloride (KCl), nitric acid (HNO_3) and Potassium bicarbonate ($KHCO_3$) from Beijing Chemical Work, urea (CH_4N_2O) and Iron chloride ($FeCl_3$) from Sinopharm Chemical Reagent Co. Nafion solution (5 wt %) was obtained from Sigma-Aldrich. All chemicals were used as delivered without further treatment. Carbon paper was purchased from CeTech Co., Ltd. Platinum wire (Premion, 99.997%). All reagents were of analytical grade and used without further purification. Deionized water (18.2 MΩ·cm) was used in all solution preparations. Nitrogen (N_2, 99.999%) and Carbon dioxide (CO2, 99.999%) were purchased from Junyang Co.,

Instrumentation: High resolution transmission electron microscopy (HRTEM) was performed using a JEOL JEM-2100 electron microscope with an operating voltage of 200 kV. HAADF-STEM images were obtained on a JEOL LEM 2200FS/TEM, equipped with a CEOS probe corrector. X-ray diffraction (XRD) measurements were performed using a Rigaku-D/MAX-PC 2500 X-ray powder diffractometer with Cu Kα X-ray source. Photoelectron spectroscopic (XPS) measurements were performed on an AXIS Ultra DLD (Kr atos company) using a monochromic Al X-ray source. The Raman spectrum was obtained on a laser confocal Raman spectroscopy (Labram-010, Horiba-JY) employing the Nd: YAG laser wavelength of 633 nm). The final Zn contents in the catalysts were obtained from ICP-MS (ICAP-6000, Thermo Fisher Scientific).The Brunauer–Emmett–Teller (BET) surface areas and pore volumes were obtained from 77 K N2 sorption isotherms using ASAP 2020 instrument.1H-NMR was performed on a BRUKER AVANCE-III 500 HD (Switzerland). Electrochemical experiments were performed

using a CHI 750E electrochemical work station (CH Instruments, Chenhua Co., Shanghai, China).

Preparation of Catalysts: *Preparation of Fe-SAC Catalyst*: 1gm of black carbon and then 3ml of 2mg/ml solutions of $FeCl_3$ with 50 mL H_2O were added to round-bottom flask by ultrasonicating the mixture for 2-3 min, and stirred during refluxing at 80 °C for 8 hours, then dried at 60 °C overnight. The dried powder was well mixed with 6gm Melamine in an agate mortar by repeated grinding. The obtained sample was then first pyrolyzed at 550°C for 4 hr under argon atmosphere with flow rate of 100 mL min^{-1} with ramp rate of 5°C/min then 700-900 °C for 1 h under argon atmosphere with flow rate of 100 mL min^{-1} at 10°C/min ramp rate. The obtained powders were washed in 1M HCl for 6hrs. The final powders were dried in vacuum oven at 60°C overnight. The optimal one was named as Fe-SACs (obtained with conditions: 800 °C for pyrolysis, mass ratio of BP : Melamine = 1:6)

Preparation of N-C Catalyst: Carbon black was mixed with melamine (mass ratio of BP: melamine = 1:6), and the mixtures was first pyrolyzed at 550°C for 4 hrs under argon atmosphere with ramp rate of 5°C/min. Then the obtained powder was pyrolyzed for the second time at 800 °C for 1 h under argon atmosphere with flow rate of 100 mL min^{-1} with ramp rate of 5°C/min. The obtained powders were washed in 1M HCl for 6hrs. Then the pyrolyzed powder was collected and denoted as N-C. Similarly, Fe-C was obtained without melamine and Fe-nanoparticle was obtained with similar procedure by triplicating the Fe precursor

Characterization: TEM images and EDX elemental mapping were performed on Tecnai G2 F20 S-TWIN with an acceleration voltage of 200 kV. HAADF-STEM images were obtained on a Cs-corrected FEI Titan G2 60-300 Microscope operated at 300 kV. Probe Cs corrector was applied

to get better spatial resolution. X-ray diffraction (XRD) patterns were recorded on D/MAX-TTRIII (CBO) (Rigaku Corporation) with Cu Kα radiation (λ=1.54 Å) at a scanning rate of 5° min^{-1}. The microstructure was studied by Raman spectra using Renishaw in Via Raman microscope with 514 nm laser excitation. X-ray photoelectron spectroscopy (XPS) was conducted on a Thermo Scientific ESCALAB 250 Xi XPS system, in which the analysis chamber pressure was 1.5×10^{-9} mbar and the size of the X-ray spot was 500 um. Specific surface area was measured at −196 °C with a Micromeritics ASAP 2010 analyzer and calculated based on a Brunauer–Emmett–Teller (BET) method. The inductively coupled plasma mass spectrometry (ICP-MS) data were taken from NexION 300X (PerkinElmer). X-ray absorption spectra were acquired in vacuum at beamline 4B7B of the Beijing Synchrotron Radiation Facility (BSRF), the ex-situ Co K-edge X-ray absorption spectra were acquired under ambient condition in florescence mode at beamline 1W1B of BSRF, using a Si (111) double-crystal monochromator. The storage ring of BSRF was operated at 2.5 GeV with a maximum current of 250 mA in decay mode. The energy was calibrated using respective metal foil, and the intensity of the incident and transmitted X-rays was monitored by standard N_2-filled ion chambers. The powder samples were pressed to a pellet to maintain the best signal. The XAS raw data were normalized, and Fourier transformed by the standard procedures with the ATHENA program. Fitting analysis of the EXAFS (k) data was carried out using the ARTEMIS program.

Electrochemical Measurements: All electrochemical measurements were carried out using a CHI 660E potentiostat in three-electrode configuration using platinum electrode as a counter electrode and Ag/AgCl as a reference electrode. Potentials measured were converted to RHE reference scale by E (vs. RHE) = E (vs. Ag/AgCl) + 0.197 + 0.059 * pH. Catalyst ink was prepared by well dispersing 4 mg of catalyst in 1 mL of ethanol and 80 μL of 5 wt% Nafion

solutions using ultra sonication. Then 50 μL catalyst inks were uniformly loaded on 1×1 cm^2 carbon paper electrode. The electrochemical measurements for CO_2 reduction were performed in a gas-tight two-component H-cell separated by Nafion 117 cation-exchange membranes. A CO_2-saturated 0.1 M $KHCO_3$ electrolyte (pH 6.8) was used as electrolyte. A CO_2 flow of (≈25 mL/min), generated from a constant stream bubbling in the cell solution, was purged into the $KHCO_3$ solution during the measurement to remove residual air and ensure continuous CO_2 saturation. The gas products of CO_2 electrochemical reduction were detected by an online GC equipped with a thermal conductivity detector (TCD) and flame ionization detector (FID) equipped with Mol sieve 5 Å column once every 12. After 30 min continuous electrolysis, 0.9 mL of $KHCO_3$ solution was collected and mixed with 0.1 mL D_2O in an NMR tube. The mixture was analyzed on a Bruker 600 MHz ^1H NMR spectrometer with water suppression to identify the liquid products. The LSV measurements were carried out in the potential range of 0.10 to −1.2 V (vs RHE) with scan rate of 5 mV s^{-1}

DFT Simulation: Spin-polarized First-principle density functional theory (DFT) calculations were performed using the Vienna ab initio simulation package (VASP)[1–3]. The projector augmented wave (PAW) method [4] were used. The exchange-correlation effects were treated in generalized gradient approximation (GGA) with the Perdew-Burke-Ernzerhof (PBE) potential.[5] The kinetic energy cutoff was chosen to be 550 eV. Gaussian smearing method[6] was employed to determine electron occupancies with a width of 0.2 eV. The Fe-N$_4$-C$_x$ structure was constructed by using a 6 × 6 graphene supercell whose six carbon atoms were substitute by Fe-N$_4$ as shown in Fig. 4b. And all other Fe-N$_4$-C$_x$ materials employ the same supercell as shown in Fig. S12. A vacuum layer no less than 15 Å was used to eliminate the spurious interaction between adjacent graphene layers along z direction. The 3×3×1 K point in the Brillouin zone

(BZ) was used for the BZ integration. The structures were relaxed before attaching any molecules. For COOH and CO adsorption, all possible sites were considered. We found that both COOH and CO prefer the Fe sites. No atom was fixed during the relaxation. The energy and fore convergence criteria were set as 10^{-5} eV and 0.01 eV/Å, respectively. The Gibbs free energy diagrams were calculated using the computational hydrogen electrode (CHE). The Gibbs free energy of a species is calculated according to $G = E_{DFT} + E_{ZPE} + \int C_p dT - TS$ where E_{DFT} is the electronic energy calculated by DFT, E_{ZPE} is the zero point energy obtained from the vibrational frequencies of adsorbates or molecules as calculated within DFT. For an adsorbate, the changes in $\int C_p dt$ and TS are much smaller compared to the variations in E_{DFT} and E_{ZPE}. Therefore, $\int C_p dt$ and TS were assumed constant for *COOH and *CO. The $\int C_p dt$ and TS for *COOH were used as 0.096 and -0.178 eV.[8] For chemical adsorbed CO, the $\int C_p dt$ and TS were used as 0.076 and -0.153 eV[8], and for physical adsorbed CO, they were used the value of gas-phase CO, since the properties of physical adsorbed CO is more closer to those of gas-phase CO. For gas-phase molecules, the $\int C_p dt$ and TS at 298.15K were used. To account for the gas-phase errors encountered with PBE exchange-correlation functional, -0.51, +0.13, -0.08 eV correction are added to the CO, CO_2, and H_2 electronic energy, respectively. [8] The solvation effect has been considered for *COOH and chemical adsorbed *CO by stabilizing 0.25 eV and 0.1 eV respectively.[8]

Product Quantification: CO_2 gas was delivered into the cathodic compartment of the cell. Then the gas phase composition vented into gas chromatograph (GC, Shimadzu GC-2014C). The gas products were analyzed by GC every 15 min. The gas concentration was averaged over three

measurements. Liquid product was characterized by 1H NMR on Bruker AVANCE III HD 400 using a pre saturation sequence. Liquid product concentration was quantified using dimethyl sulfoxide (DMSO) as the internal standard. The faradic efficiency and turnover frequency are calculated by the equations as follows:

Faradic efficiency (FE):

$$FE_{CO} = J_{CO}/J_{total} = v_{co} \times N \times F / J_{total}$$

FE_{CO}: Faradic efficiency for CO formation;

J_{CO}: Current density for CO formation;

J_{total}: Total Current density;

v_{co}: Production rate of CO (measured by GC);

N: Number of electron transferred for product formation, which is 2 for CO;

F (Faraday constant): 96485.3 C mol^{-1};
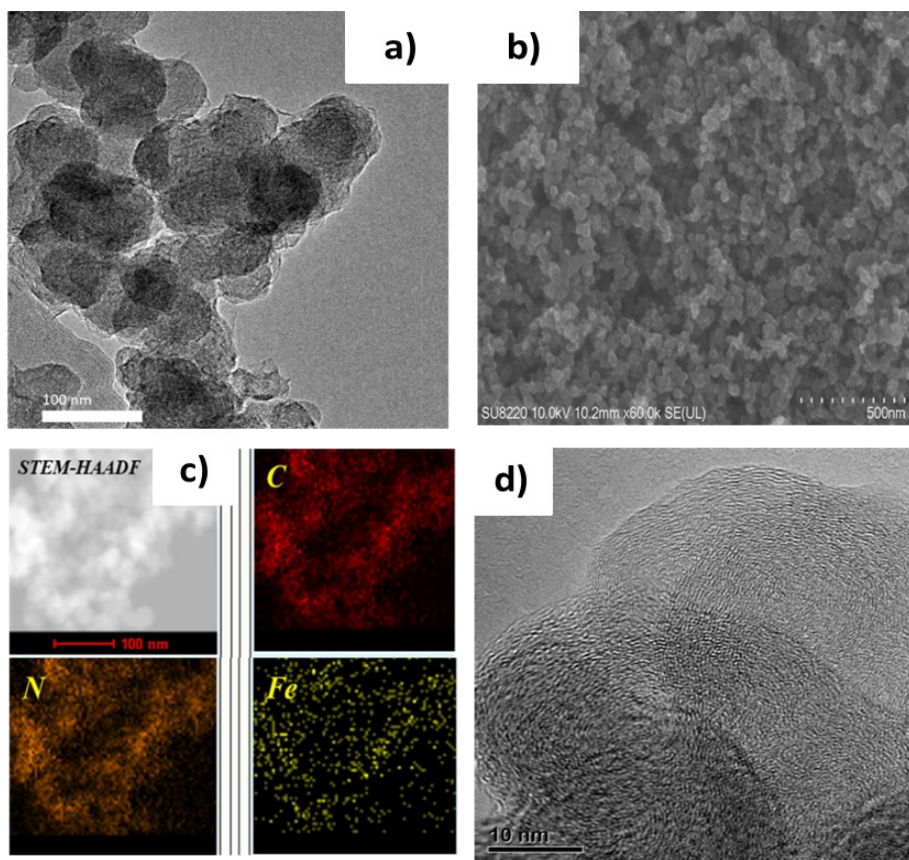
Figure S1. Morphological study: (a) Representative TEM image of Fe-SACs, (b) SEM image of Fe-SACs, (c) Elemental mapping of Fe-SACs (d), High resolution TEM image of FE-SACs
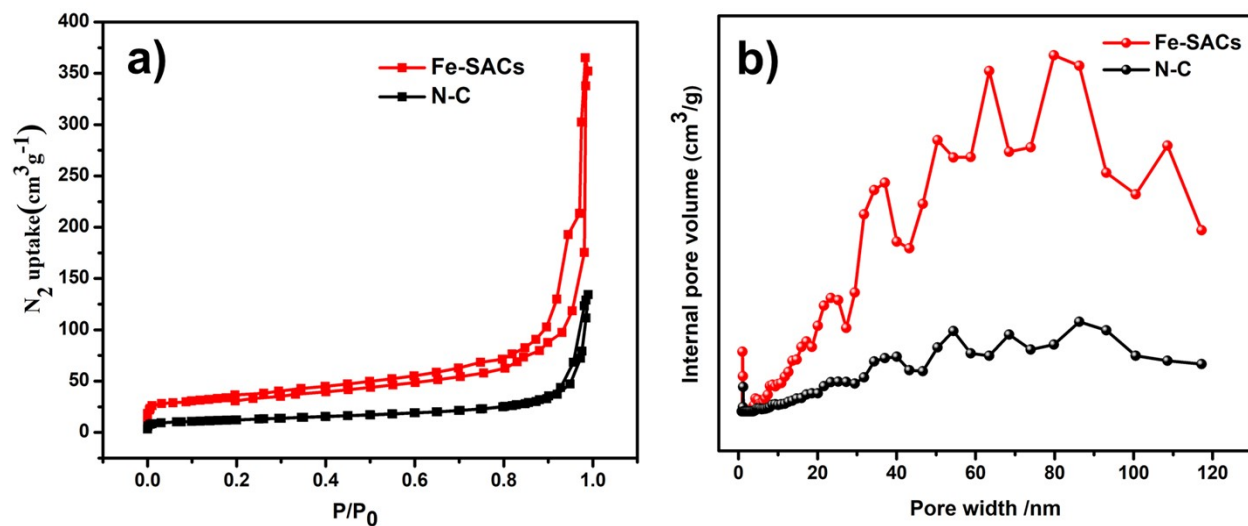
Figure S2. Brunauer-Emmett-Teller (BET) N_2 specific ad/desorption isotherm profile and pore distribution statistics. (a) N_2 adsorption/desorption isotherms of Fe-SACs and N-C. (b) Pore size distributions of Fe-SACs and N-C.
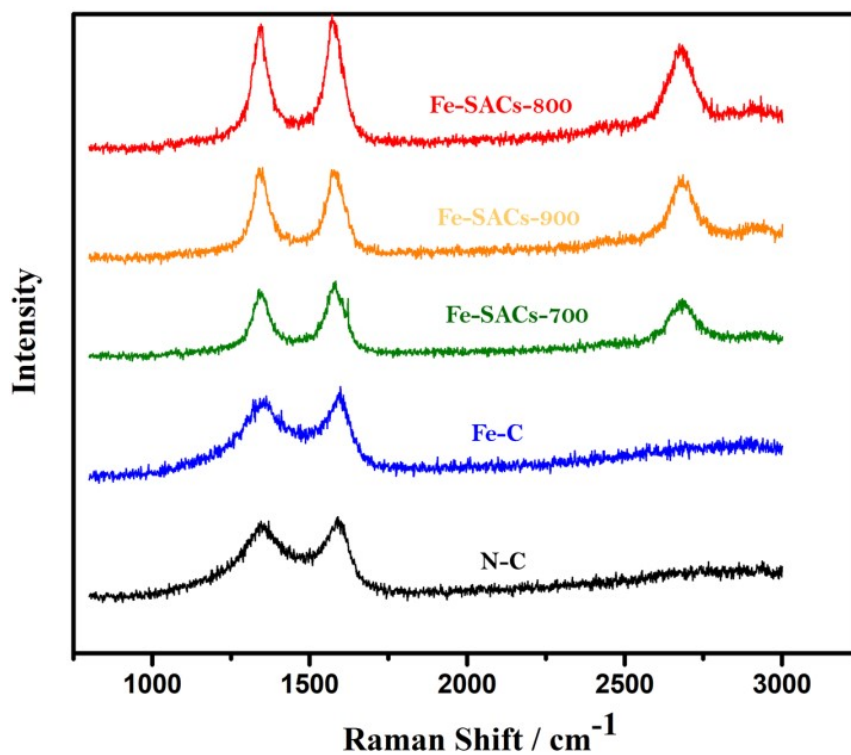

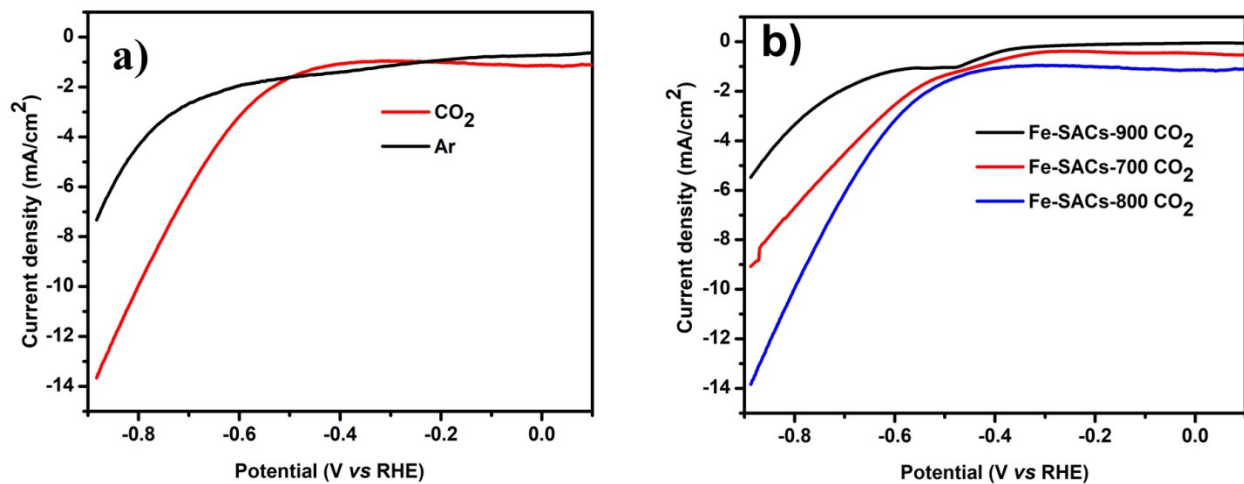**Figure S3.** . Raman spectra of Fe-SACs, Fe-C and N-C catalysts

Figure S4: LSV comparisons of (a) Fe-SACs in CO_2 saturated and Ar saturated 0.1M $KHCO_3$ electrolyte and (b) different pyrolysis temperature at cathodic sweeping rate of 5 mV s^{-1} with the same mass loading.
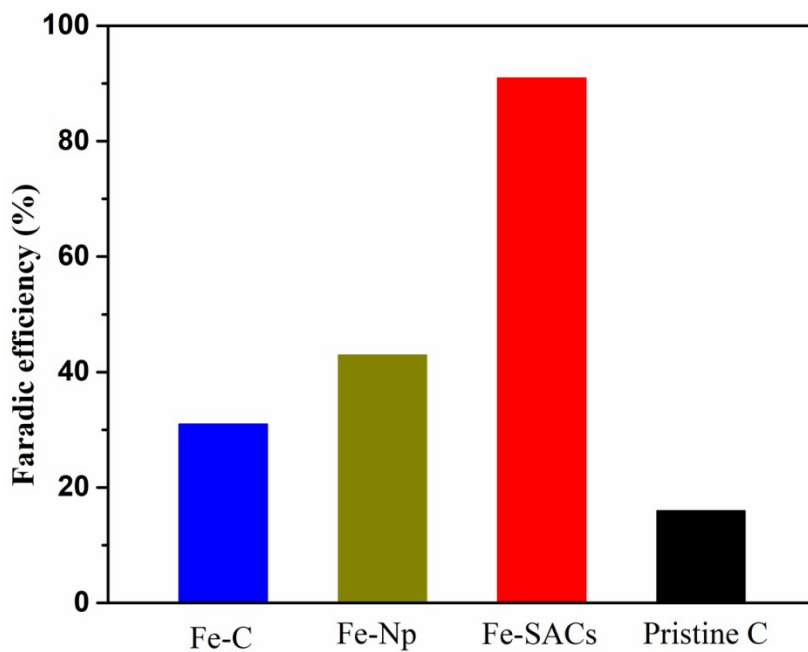

Figure S5: Comparisons of faradic efficiency of different catalysts
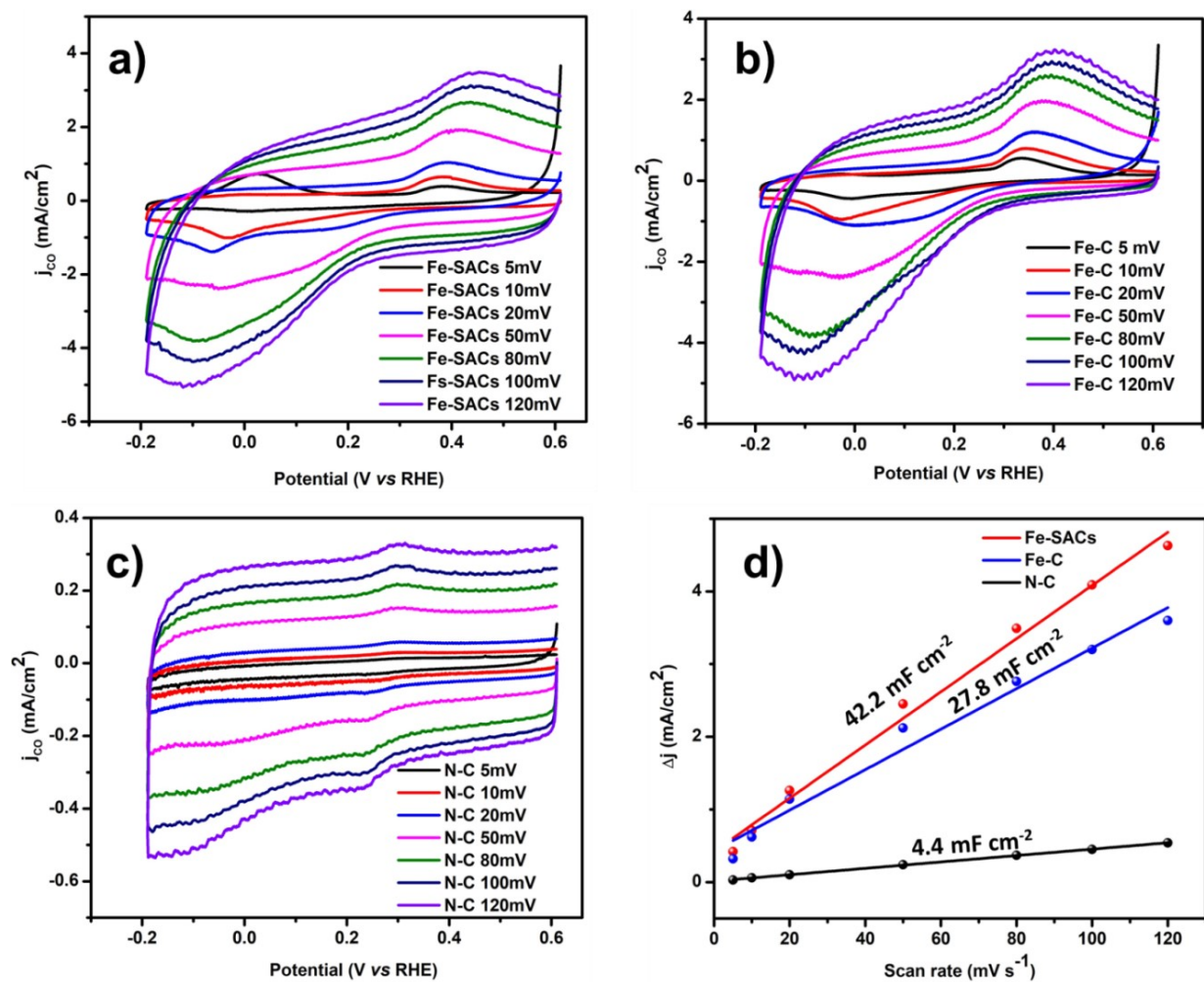
Figure S6. Cyclic voltammetry of (a) Fe-SACs, (b) Fe-C and (c) N-C catalysts conducted in Ar-saturated 0.1M KHCO$_3$ solution at scan rate 5 mV s^{-1}, 10 mV s^{-1}, 20 mV s^{-1}, 50 mV s^{-1}, 80 mV s^{-1}, 100 mV s^{-1} and 120 mV s^{-1} to determine the double layer capacity. (d) ECSA comparison among of Fe-SACs, Fe-C and N-C catalysts
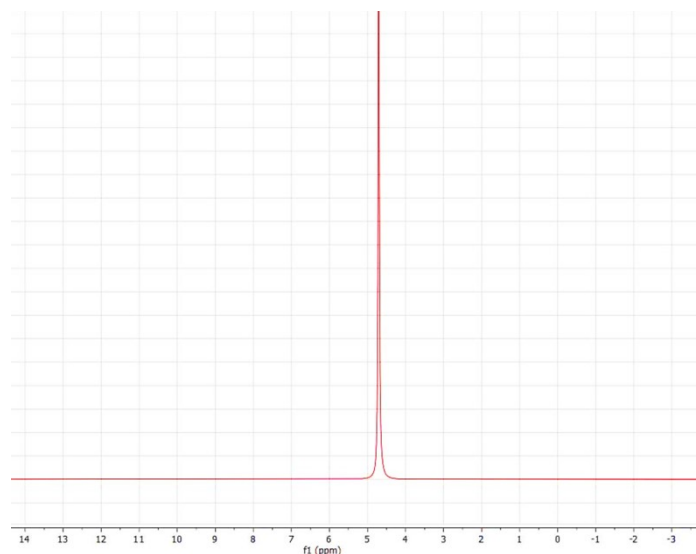
Figure S7. Representative 1H-NMR spectrum of Fe-SACs catalyst after CO_2 reduction electrolysis at -0.5 V in CO_2-saturated KHCO3 solution
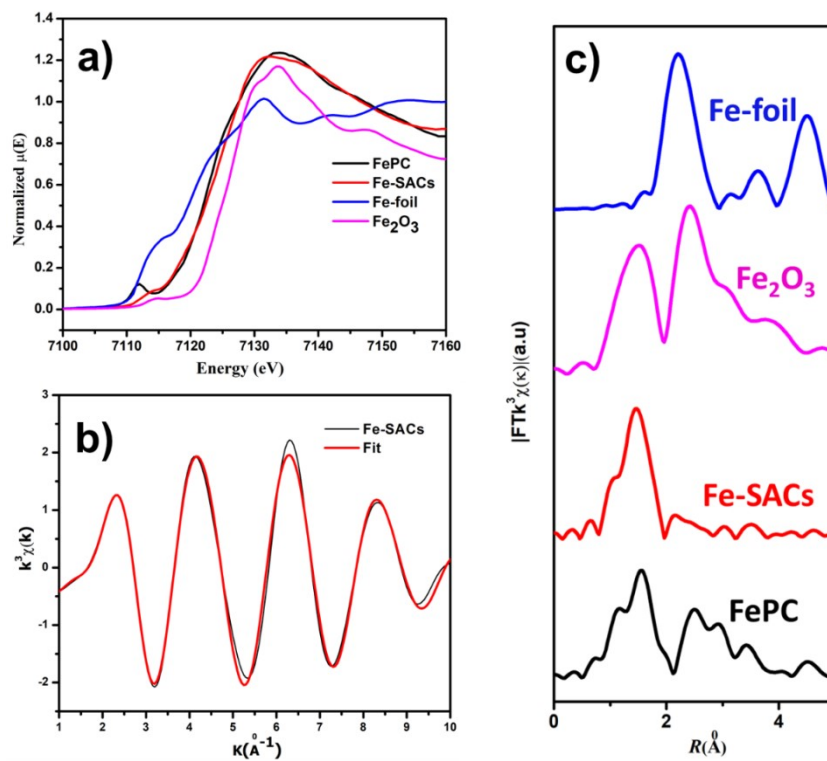

Figure S8: (a) Fe K-edge XANES spectra of Fe-SACs. (b) k-space of Fe K-edge fitting EXAFS Spectrum (black) and the fitting curves (red). and (c) Fourier transformed (FT) extended X-ray absorption fine structure (EXAFS) of these samples
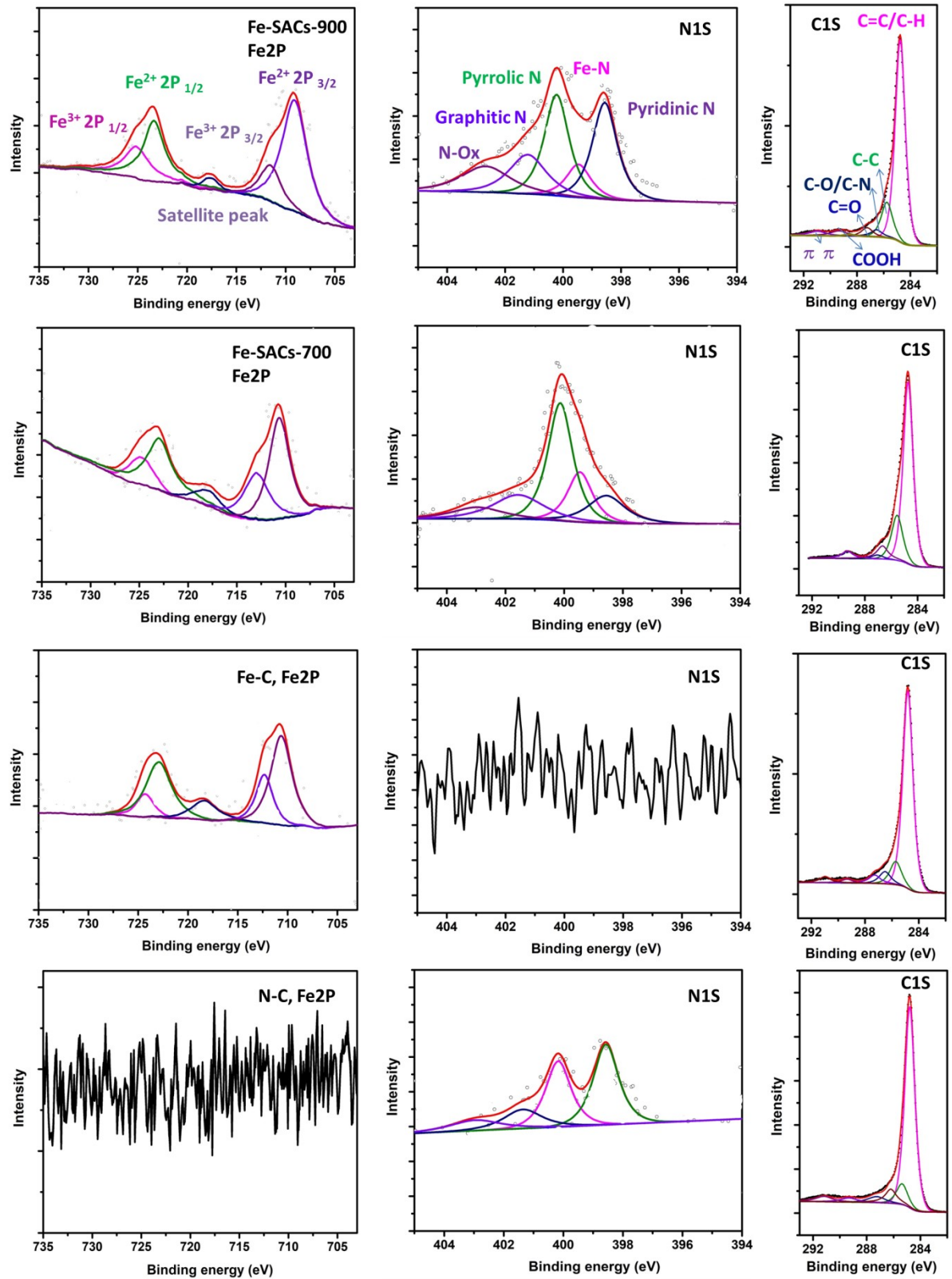
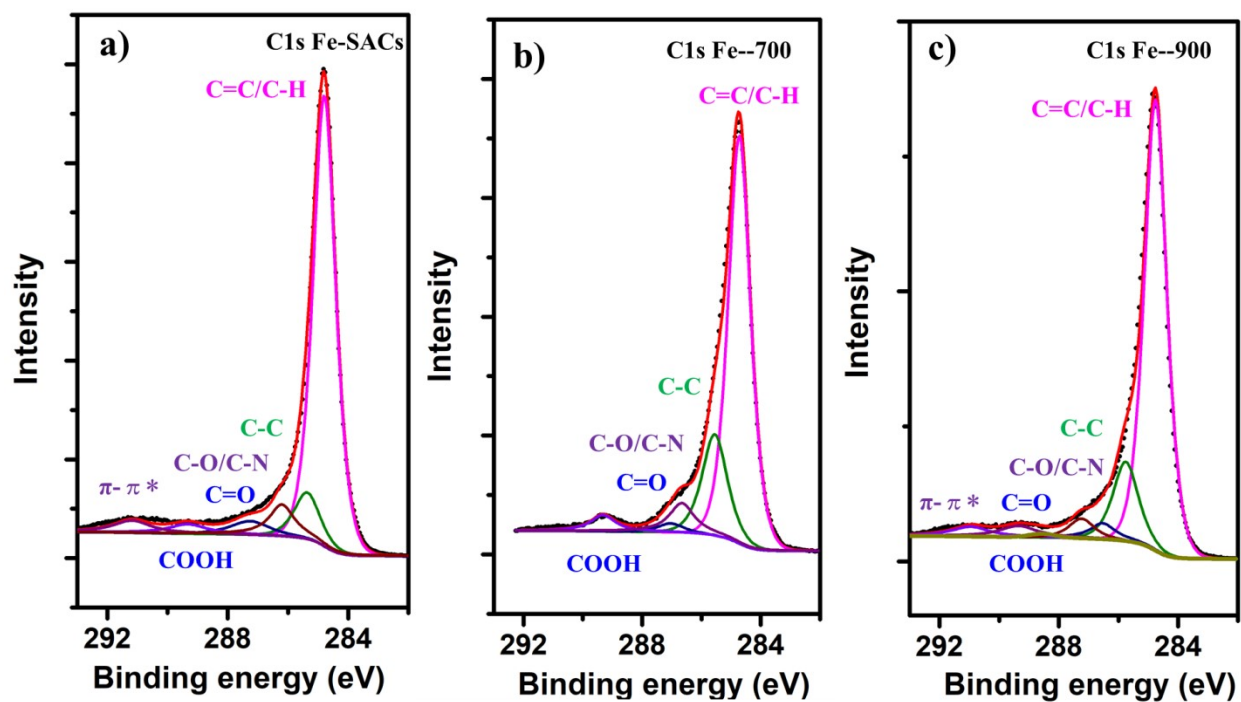**Figure S9:** XPS spectra of different Fe-SACs and control samples

Figure S10: C1s XPS spectra of different Fe-SACs catalysts
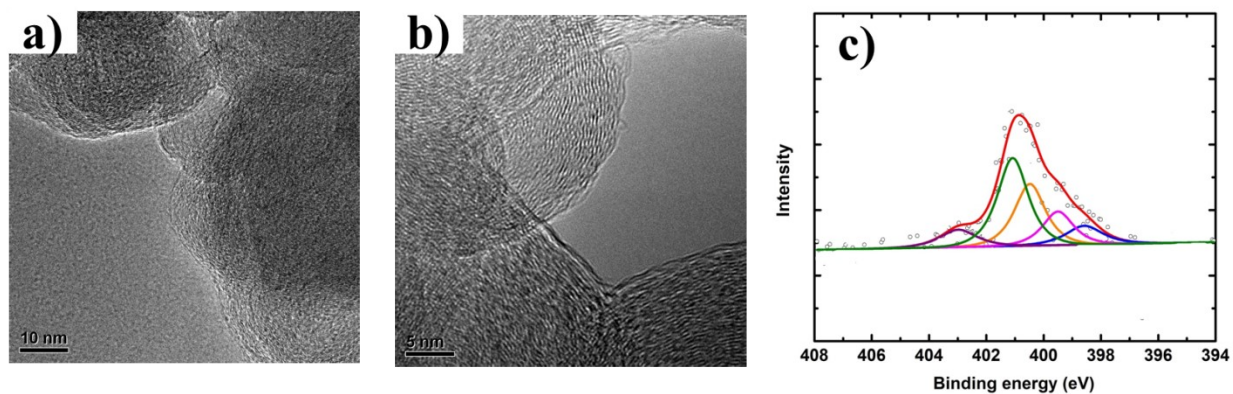
Figure S11: C1s XPS and TEM spectra after prolonged time analysis

FeN$_4$-1N-1 FeN$_4$-1N-2 FeN$_4$-1N-3

FeN$_4$-1N-4 FeN$_4$-1N-5 FeN$_4$-1N-6

FeN$_4$-2N-1 FeN$_4$-2N-2 FeN$_4$-2N-3

FeN$_4$-2N-4 FeN$_4$-2N-5 FeN$_4$

FeN$_4$-3N-1 FeN$_4$-3N-2 FeN$_4$-3N-3

FeN$_4$-3N-4 FeN$_4$-3N-5 FeN$_4$-3N-6

FeN$_4$-4N-1 FeN$_4$-4N-2 FeN$_4$-4N-3

Figure S12: Model Different configuration of graphitic N neighboring Fe-N$_4$

Figure S13: Free energy diagram of Fe-N4 with different graphitic N amount and configurations

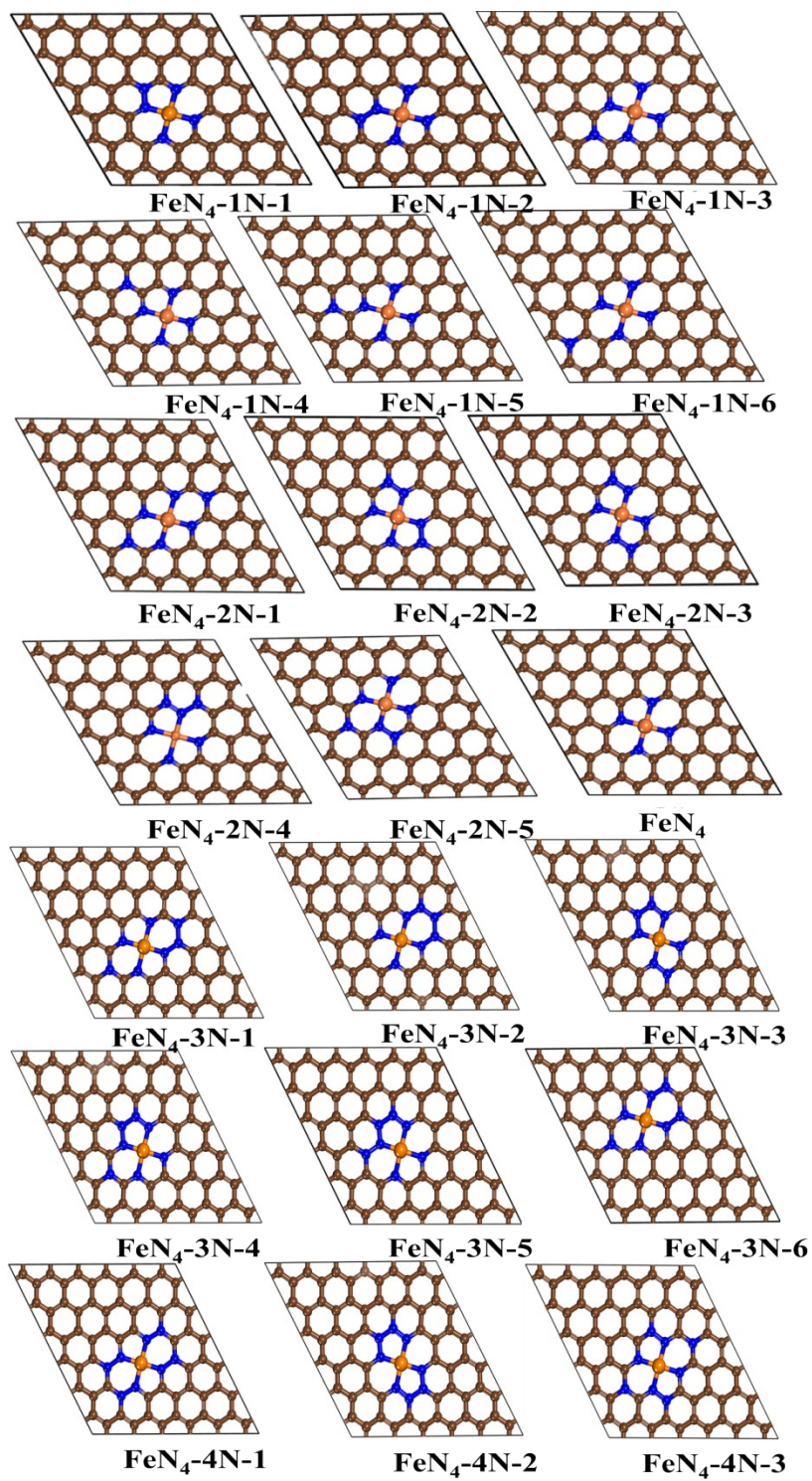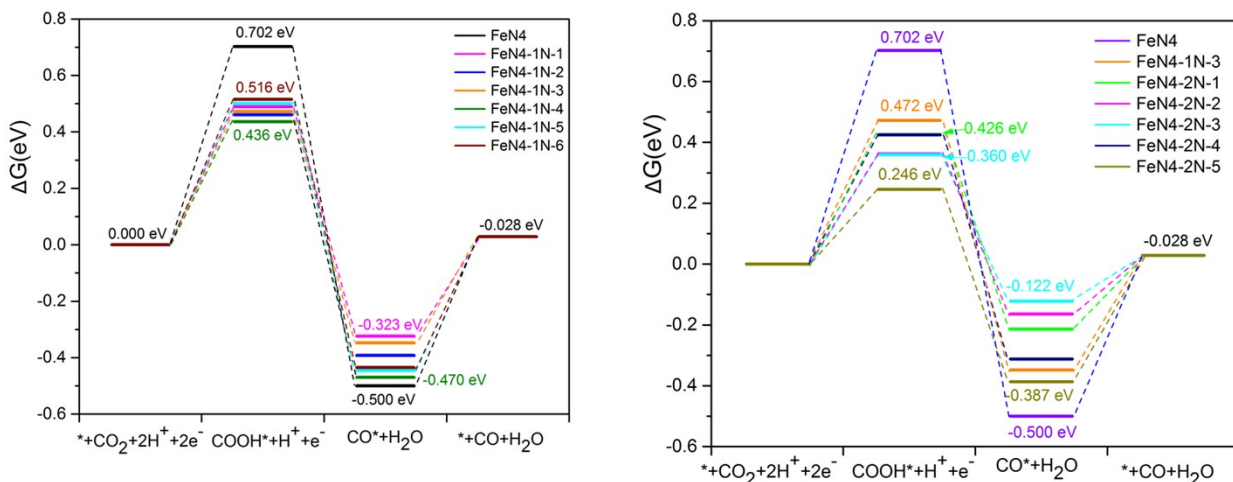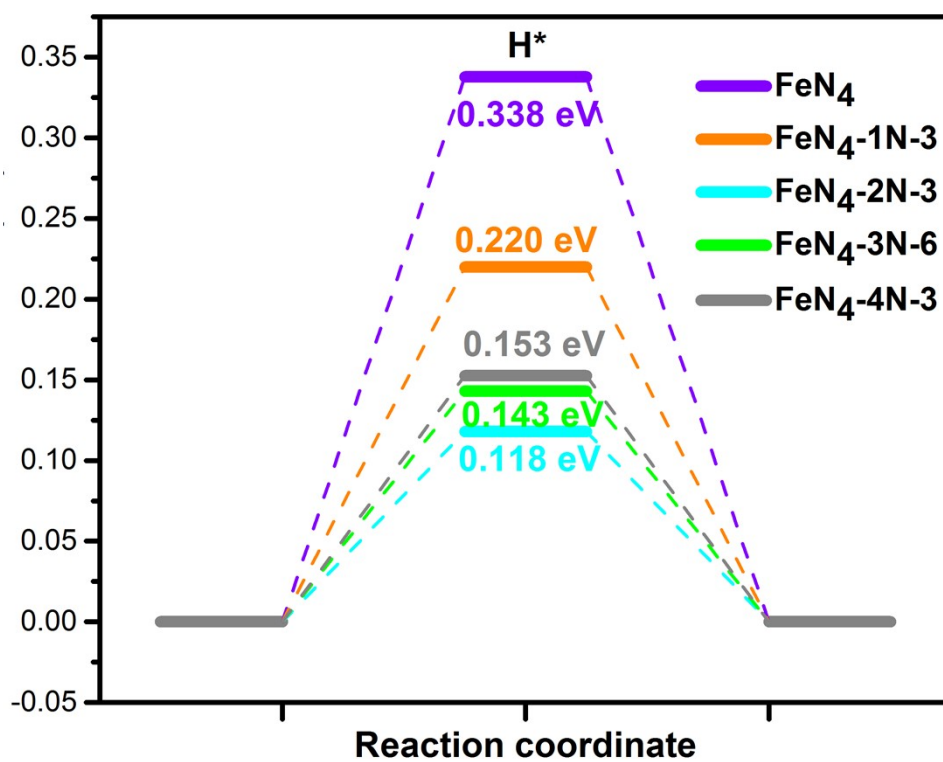**Figure S14:** Free energy diagram for the hydrogen evolution reaction (HER) on Fe–N_4 moieties embedded on carbon sheets (gray(C), Orange (Fe) Blue (N) Red (O) and light white (H).

The hydrogen evolution reaction (HER) is also studied becauce it is the main side reaction of the CO_2 reduction reaction. During the HER, the H consume one proton-electron pair on the surface of catalyst, forming the adsorbed H*, which would occupy the active sites and hinder the formation of COOH*. Therefore, the strong adsorption of H* would reduce the activity and selectivity of the catalysts. From the HER results in Figuer S14, the forming of the adsorbed H* on the studied catalysts are all not spontaneous, and they all need to overcame an energy barrier (0.118-0.338 eV). This results indicates that the adsorption of H* is not strong so that it would not occupy the active sites for a long time, *i.e.* it would not significantly weaken the activity of the catalysts. However, since the barriers of HER are not high, the selectivity maybe reduced at a certain extent. Fortunately, separation of the principal products CO and the by-products H_2 is not so difficult.

Free energy diagram for electrochemical CO2 reduction to CO on Fe–N4 moieties embedded on carbon sheets inset: optimized geometries of reaction intermediates (gray(C), Orange(Fe) Blue(N) Red(O) and light white (H)

Table: S1: N content of different temperature pyrolyzed catalysts

Sample	ID/IG ratio	Fe(At %)	Nitrogen %	Fittings of N moieties/atom%				
				pyridinic	pyrrolic	M-Nx	N-Ox	Graphitic
Fe-SACs	1.01	0.18	1.16	29.4	25.2	14.4	10.6	20.2
Fe-SACs-700	1.16	0.24	1.23	29.6	30.1	15.8	8	17.1
Fe-SACs-900	1.02	0.11	0.93	28.2	24.1	13.5	13.1	20.5
N-C	1.21	-	1.86	41.1	33.6	-	10.6	14.5
Fe-SACs after 35 hr rxn		0.15	0.98	27.3	22.6	12.7	13.6	23.2

Table S2: EXAFS fitting result of the Fe-N$_4$ SACs catalyst.

The data range adopted for data fitting in k-space (Δk) and R space (ΔR) are 2-11.426 Å^{-1}and 1-3 Å, respectively.

Sample	Shell	N	R/Å (EXAFS)	Debye-Waller factor $\Delta \sigma^2 (\times 10^{-3} \text{ Å}^2)$	ΔE_0(eV)	R factor
Fe-C-N	Fe-N	3.6 $\pm$ 0.5	1.971	9 $\pm$ 0.59	-9.8	8.6

N, coordination number; R, interatomic distance; EXAFS, extended X-ray absorption fine structure

Table S3: Bader charge of *COOH and *CO on the five catalysts

Catalysts	*COOH/e	*CO/e
FeN_4	0.2919	0.2227
FeN_4-1N-3	0.384	0.2683
FeN_4-2N-3	0.3603	0.1622
FeN_4-3N-4	0.3311	0.2447
FeN_4-4N-2	0.3014	0.2039

Table S4: CO_2RR performances comparison of FeN_4-Graphitic N catalyst with some typical catalysts for CO2RR

Catalysts	Electrolyte	Maximum FE_{CO}	Potential RHE	Ref.
Fe-SACs	**0.1 M KHCO₃**	**91%**	**-0.50V**	**This work**
HMG	0.1 M KHCO₃	96.6%	-0.46V	10
Fe-N-C	0.1 M KHCO₃	80%	-0.60V	11
Fe/NG-750	0.1 M KHCO₃	80%	-0.57V	12
Ni-N-G	0.1 M KHCO₃	90%	-0.70V	13
A-Ni-NSG	0.5 M NaHCO₃	97%	-0.72V	14
Co-N₂	0.5 M NaHCO₃	94%	-0.63V	15
CoPc/CNT	0.1 M KHCO₃	92%	-0.63V	16
FeN₄/Graphitic	0.1 M NaHCO₃	97%	-0.60V	17
ZnNx/C	0.1 M KHCO₃	95%	-0.43V	18
Fe-N-C	0.1 M KHCO₃	86%	-0.50V	19
Ni-N-C	0.1 M KHCO₃	97%	-0.80V	19
NCNT-3-700	0.5 M NaHCO₃	90%	-0.90V	20
(Cl, N)-Mn/G	0.5 M KHCO₃	97%	-0.50V	21

References

1. G. Kresse and J. Hafner, Phys. Rev. B, 1993, 47, 558.

2. G. Kresse and J. Furthmüller, Comput. Mater. Sci., 1996, 6, 15.

3. G. Kresse and J. Hafner, Phys. Rev. B, 1994, 49, 14251.

4. G. Kresse and D. Joubert, Phys. Rev. B, 1999, 59, 1758.

5. J. P. Perdew, K. Burke and M. Ernzerhof, Phys. Rev. Lett., 1996, 77, 3865.

6. M. Methfessel and A. T. Paxton, Phys. Rev. B, 1989, 40, 3616.

7. S. Grimme, J. Antony, S. Ehrlich, and S. Krieg, J. Chem. Phys. 2010, 132, 154104

8. A. A. Peterson, F. Abild-Pedersen, F. Studt, J. Rossmeisl, J. K. Norskov, Energy Environ. Sci. 2010, 3, 1311.

9. D. Karapinar, N.T. Huan, N. R. Sahraie, J. Li, D. Wakerley, N. Touati, S. Zanna, D. Taverna, L. H. G. Tizei, A.Zitolo, F. Jaouen, V.Mougel, and M. Fontecave, Angew. Chem., Int. Ed. 2019, 58, 15098.

10. Z. Huinian , L. Jing, X. Shibo, D. Yonghua, H. Xiao, W. Junying, X. Haomin, W.Gang, Z. Jia ,L. Jiong, and W. Junzhong Angew. Chem. Int. Ed. 2019, 58, 14871– 14876.

11. A. S. Varela, N. Ranjbar Sahraie, J. Steinberg, W. Ju, H.- S. Oh, P. Strasser, Angew. Chem. Int. Ed. 2015, 54, 10758 – 10762.

12. C. Zhang, S. Yang, J. Wu, M. Liu, S. Yazdi, M. Ren, J. Sha, J. Zhong, K. Nie, A. S. Jalilov, Z. Li, H. Li, B. I. Yakobson, Q. Wu, E. Ringe, H. Xu, P. M. Ajayan, J. M. Tour, Adv. Energy Mater. 2018, 8, 1703487.

13. P. Su, K. Iwase, S. Nakanishi, K. Hashimoto, K. Kamiya, Small 2016, 12, 6083 – 6089.

14. H. B. Yang, S.-F. Hung, S. Liu, K. Yuan, S. Miao, L. Zhang, X. Huang, H.-Y. Wang, W. Cai, R. Chen, J. Gao, X. Yang, W. Chen, Y. Huang, H. M. Chen, C. M. Li, T. Zhang, B. Liu, Nat. Energy 2018, 3, 140 – 147.

15. X. Wang, Z. Chen, X. Zhao, T. Yao, W. Chen, R. You, C. Zhao, G. Wu, J. Wang, W. Huang, J. Yang, X. Hong, S. Wei, Y. Wu, Y. Li, Angew. Chem. Int. Ed. 2018, 57, 1944 – 1948.

16. X. Zhang, Z. Wu, X. Zhang, L. Li1, Y. Li, H. Xu, X. Li, X. Yu, Z. Zhang, Y. Liang and H. Wang, Nat. Commun. 2017, 8, 14675.

17. L. Chuhao, W. Yue, S. Kaian, F. Jinjie, H. Aijian, P. Yuan, C. C. Weng, Z. Zewen, Z. Zhongbin, Y. Qiuhua, L. X. Huolin, Z. Chao, Z. Jiangwei, X. Hai Xiao, C. Chen and L. Yadong , Chem 7, 1297–1307.

18. F. Yang, P. Song, X. Liu, B. Mei, W. Xing, Z. Jiang, L. Gu, and W. Xu, Angew. Chem., Int. Ed. 2018, 57, 12303.

19. L. T. Menisa, C. Ping, L. Chang , Q. Xueying , Z. Yonglong, H. Jianyu, Z. Yin , G. Yan and T. Zhiyong, *Nanoscale*, 2020,**12**, 16617-16626.

20. J. Xu, Y. Kan, R. Huang, B. Zhang, B. Wang, K.-H. Wu, Y. Lin, X. Sun, Q. Li, G. Centi, D. Su, ChemSusChem 2016, 9, 1085 – 1089.

21. B. Zhang, J. Zhang, J. Shi, D. Tan, L. Liu, F. Zhang, C. Lu, Z. Su, X. Tan, X. Cheng, B.Han, L. Zheng and J. Zhang, Nat. Commun. 2019, 10, 2980.